PERGAMON

International Journal of Heat and Mass Transfer 46 (2003) 613–629

International Journal of HEAT and MASS TRANSFER

www.elsevier.com/locate/ijhmt

Bifurcation and stability of combined free and forced convection in rotating curved ducts of square cross-section

Tianliang Yang [a,*], Liqiu Wang [b]

[a] Department of Mechanical Engineering, University of Kentucky, Lexington, KY 40506, USA
[b] Department of Mechanical Engineering, The University of Hong Kong, Pokfulam Road, Hong Kong

Received 10 August 2001; received in revised form 7 August 2002

Abstract

A numerical study is made on fully developed bifurcation structure and stability of combined free and forced convection in a rotating curved duct of square cross-section. The solution structure is determined as the variation of a parameter indicating the magnitude of buoyancy force. Steady solution structure is very complicated. Flow and temperature fields on various solution branches are identified to be symmetric/asymmetric multi-cell patterns. Dynamic responses of multiple solutions to finite random disturbances are examined by direct transient computation. *Five types* of physically realizable solutions are identified numerically. They are stable steady 2-cell solution, stable steady multi-cell solution, periodic oscillation, chaotic oscillation and *symmetry-breaking oscillation led by sub-harmonic bifurcation (period doubling)*. Among them, *three kinds of stable steady solutions are found to co-exist within a range of parameters*. In addition, temporal periodic and chaotic oscillations can also co-exist in another range of parameters. Furthermore, sub-harmonic bifurcation *is identified to be another route to chaos*. Spectral analysis is used to demonstrate the presence of additional frequencies for the case of sub-harmonic bifurcations. Results show that symmetry-breaking oscillation driven by sub-harmonic bifurcations appear to be identical with the mode observed in Lipps [J. Fluid Mech. 75 (1976) 113], McLaughlin and Orszag [J. Fluid Mech. 122 (1982) 123], and Gollub and Benson [J. Fluid Mech. 100 (1980) 449] for problem of free convection between flat horizontal plates.

1. Introduction

We study fully-developed multiplicity and dynamic responses of multiple solutions numerically by finite-volume/Euler–Newton continuation for mixed convection in ducts of square cross-section with streamwise curvature, spanwise rotation in either positive or negative direction, and wall heating/cooling (Fig. 1 with (R, Z, ϕ) as the radial, spanwise and streamwise directions, respectively). A positive rotation gives raises to a Coriolis force in the cross plane (RZ-plane) directed along positive *R*-direction and vice versa.

There are a host of areas where such flows and transport phenomena are of practical importance and where relevant issues are raised. Cooling ducts of rotating power machinery such as gas/steam turbines and electric generators, rotating heat exchangers represent some examples for flow and heat transfer in rotating curved ducts. In order to calculate the pumping power needed for such devices, it is important to know the pressure drop in rotating curved ducts. Because secondary flows can enhance heat and mass transfer, knowledge of magnitude of this effect in different ranges of operating parameters is important in designing and operating these devices. To avoid or reduce the flow-induced vibration and noise, we need to know when

* Corresponding author. Tel.: +1-859-257-6336; fax: +1-859-257-3304.
E-mail address: tlyang@engr.uky.edu (T. Yang).

0017-9310/03/$ - see front matter © 2002 Elsevier Science Ltd. All rights reserved.
PII: S0017-9310(02)00329-0

Nomenclature

a	duct width/height
De	Dean number
Dk	modified Dean number
$L1$	dimensionless variable indicating the effect of rotation
p	dimensionless pressure
Pr	Prandtl number of the fluid
R_c	curvature radius
Re	Reynolds number
r, z	dimensionless coordinates
R, Z, ϕ	coordinates
u, v, w	dimensionless velocity components in directions of R, Z, and ϕ

Greek symbols

θ	dimensionless temperature of the fluid
σ	curvature ratio of the channel
τ	dimensionless time
ψ_{max}	maximum of absolute values of secondary flow stream function

temporal oscillation appears. The present work can acquire a better understanding of these practical issues.

Early works on rotating curved duct flows were constrained to two simplified limiting cases with strong or weak rotations. Ludwieg [4] developed a solution based on a momentum integral method for the isothermal flow in a square duct with a strong spanwise rotation. Miyazaki [5,6] examined the mixed convection in a curved circular/rectangular duct with spanwise rotation and wall heating by a finite difference method. Because of the convergence difficulties with the iterative method used, Miyazaki's work was constrained to the case of weak curvature, rotation and heating rate. As well, all the works employ a steady model for fully developed laminar flow with a positive rotation of the duct. Since the solution is only for the asymptotic cases, secondary flow revealed by these early works consists of only one pair of counter-rotating vortices in the cross-plane. The interaction of secondary flow with pressure-driven streamwise flow shifts the location of maximum streamwise velocity away from the center of duct and in the direction of secondary velocity in the middle of duct.

More comprehensive studies have been made in recent years by Wang and Cheng [7] and Daskopoulos and Lenhoff [8] for a circular tube, Matsson and Alfredsson [9,10] and Guo and Finlay [11] for a high-aspect-ratio rectangular duct, and Wang and Cheng [12,13], Selmi et al. [14] and Selmi and Nandakumar [15] for the square and rectangular ducts with a low-aspect-ratio. All the works are for steady fully developed flows. Wang and Cheng [7] developed an analytical solution for rotating curved flow with effect of heating or cooling that allows analyzing the solution structure. Detailed flow structures and heat transfer characteristics were examined numerically by Wang and Cheng [13]. The rotating curved flows were visualized using smoke injection method by Wang and Cheng [12]. Daskopoulos and Lenhoff [8] made the first bifurcation study numerically under the small curvature and the symmetry condition imposed along the tube horizontal central plane. Matsson and Alfredsson [9] presented the first and comprehensive linear stability analysis. Matsson and Alfredsson [10] reported an experimental study, by hot-wire measurements and smoke visualization, of the effect of rotation on both primary and secondary instabilities. Using a linear stability theory and spectral method, Guo and Finlay [11] examined the stability of streamwise oriented vortices to 2-D, spanwise-periodic disturbances (Eckhaus stability). Detailed bifurcation structure and linear stability of solutions was determined numerically by Selmi et al. [14] and Selmi and Nandakumar [15] without imposing the symmetric boundary conditions.

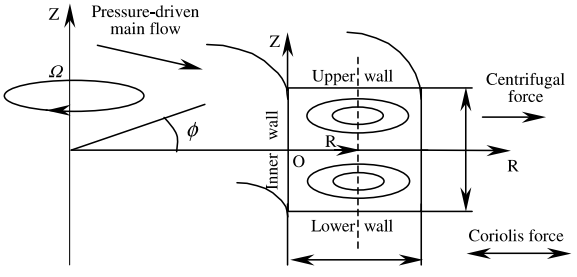

Fig. 1. Physical problem and coordinate system.

It is the relative motion between bodies that determines the performances such as friction and heat transfer characteristics. Duct rotation introduces both centrifugal and Coriolis forces in the momentum equation describing the relative motion of fluids with respect to duct. For isothermal flows of a constant property fluid, the Coriolis force tends to produce vorticity while centrifugal force is purely hydrostatic, analogous to Earth's gravitational field [13]. When a temperature-induced variation of fluid density occurs for non-isothermal flows, both Coriolis and centrifugal-type buoyancy forces could contribute to the generation of vorticity [13]. These two effects of rotation either enhance or counteract each other in a non-linear manner depending on the direction of duct rotation, the direc-

tion of wall heat flux and the flow domain. As well, buoyancy force is proportional to square of the rotation speed while Coriolis force increases proportionally with the rotation speed itself [13]. Therefore, the effect of system rotation is more subtle and complicated and yields new, richer features of flow and heat transfer in general, bifurcation and stability in particular, for non-isothermal flows. While some of such new features are revealed by recent analytical and numerical works [7,13], there is no known study on bifurcation and stability of mixed convection in rotating curved ducts.

We note that all previous analytical/numerical studies of stability are limited to linear stability and some special disturbances. While linear stability analysis is efficient in terms of the computation efforts required, it suffers three fundamental defects. First, it is not applicable to a finite disturbance. With a finite disturbance, a so-called stable solution based on linear stability may not be always stable. Second, it may not be so relevant for comparison with experiments. Because of the difficulty in controlling disturbances in experiments, experimental results of stability such as those in Matsson and Alfredsson [10] and Wang and Cheng [12] are essentially for finite random disturbances. Finally, linear stability analysis provides no answer to the questions related to the dynamic behavior of solutions, including how flows approach a stable solution after a disturbance, what happens to an unstable solution after a disturbance, whether all unstable solutions at a given set of parameters respond to disturbances in the same way, and whether disturbances lead an unstable solution to stable one at the same parameter value. Clearly, a fully transient computation is necessary to examine dynamic responses of the multiple solutions to the finite random disturbances. Such a computation is also capable of capturing the phenomena related to the transition to turbulence such as oscillation solution, periodic doubling, intermittency, and chaotic oscillation.

In previous numerical studies [8,14,15], branch stability is often determined by stability of one point on the branch. This is partly due to the fact that computation of complete eigenvalue spectrum along solution branches is a computationally expensive process and partly due to the assumption that stability of solutions along a solution branch is unchanged without passing limit/bifurcation points in the literature. However, based on bifurcation and stability theory, such a change in stability is possible. Therefore, a more detailed and careful stability analysis is desirable to observe the gain and loss of flow stability along solution branches without passing limit/bifurcation points.

The present work is a relatively comprehensive study on bifurcation structure and stability of multiple solutions for laminar mixed convection in a rotating curved duct of square cross-section (Fig. 1). The governing differential equations in primitive variables are solved for detailed bifurcation structure by a finite-volume/Euler–Newton continuation method with the help of bifurcation test function, branch switching technique and parameterization of arc-length or local variable. Transient calculation is made to examine the response of every solution family to finite random disturbances. Power spectra are constructed by the Fourier transformation of temporal oscillation solutions to confirm the chaotic flow. We restrict ourselves to the hydrodynamically and thermally fully-developed region and two-dimensional disturbances. So far, a detailed 3-D numerical computation of flow bifurcation and stability is still too costly to conduct. A 2-D model is still useful for a fundamental understanding of rotating curved duct flows. However, our assumption of fully developed flow limits our analysis to the one preserving streamwise symmetry. There may be further bifurcation to flows that breaks this symmetry and that cannot be found in the present work.

2. Governing parameters and numerical algorithm

Consideration is given to a hydrodynamically and thermally fully developed laminar flow of viscous fluid in a square duct with streamwise curvature, spanwise rotation, and wall heating or cooling at a constant heat flux (Fig. 1). The geometry is toroidal and hence finite pitch effect is not considered. The rotation can be positive or negative at a constant angular velocity. The duct is streamwisely and peripherally uniformly heated or cooled with a uniform peripheral temperature. The properties of fluid, with the exception of density, are taken to be constant. Usual Boussinesq approximation is used to deal with the density variation.

Consider a non-inertial toroidal coordinate system (R, Z, ϕ) fixed to the duct rotating with a constant angular velocity about O′Z′ axis, as shown in Fig. 1. We may obtain the governing differential equations, in the form of primitive variables (i.e. u, v, w, p, and θ), governing fully-developed mixed convection based on conservation laws of mass, momentum and energy. The boundary conditions are non-slip and impermeable, streamwise uniform wall heat flux and peripherally uniform wall temperature at any streamwise position. The proper scaling quantities for non-dimensionalization are chosen based on our previous experience [13]. The formulation of the problem is on full flow domain without imposing symmetric boundary conditions to perform a thorough numerical simulation. The readers are referred to Yang and Wang [16] and Wang and Cheng [13] for the details of mathematical formulation of the problem.

The dimensionless governing equations contain five dimensionless governing parameters: one geometrical parameter σ (the curvature ratio defined by a/R_c, the

ratio of duct width/height a over the radius of the curvature R_c, representing the degree of curvature), one thermophysical parameter Pr (the Prandtl number, representing the ratio of momentum diffusion rate to that of the thermal diffusion), and three dynamical parameters Dk, $L1$ and $L2$ defined in Wang and Cheng [13]. The pseudo Dean number Dk is the ratio of the square root of the product of inertial and centrifugal forces to the viscous force and characterizes the effect of inertial and centrifugal forces. $L1$ represents the ratio of the Coriolis force over the centrifugal force, characterizing the relative strength of Coriolis force over the centrifugal force. $L2$ is the ratio of the buoyancy force over the centrifugal force and represents the relative strength of the buoyancy force. A positive (negative) value of $L1$ is for the positive (negative) rotation. A positive (negative) value of $L2$ indicates the wall heating (cooling). In the present work, we set $\sigma = 0.2$ (typically used in cooling systems of rotor drums and conductors of electrical generators) and $Pr = 0.7$ (a typical value for air) to study the effects of three dynamical parameters on the multiplicity and stability. While results regarding the effects of Dk and $L1$ are also available, we focus on the effects of $L2$ at $Dk = 300$ and $L1 = 28$ in the present paper due to limited space.

The governing differential equations are discretized by finite volume method to obtain discretization equations. The discretization equations are solved for parameter-dependence of velocity, pressure and temperature fields by the Euler–Newton continuation method with the solution branches parameterized by $L2$, the arc-length or the local variable. The starting points of our continuation algorithms are the three solutions at $Dk = 300$, $L1 = 28$ and $L2 = 0$ from our study of the effects of Dk and $L1$. The bifurcation points are detected by the test function developed by Seydel [17,18]. The branch switching is made by a scheme approximating the difference between branches proposed by Seydel [17,18]. The dynamic responses of multiple solutions to the 2-D finite random disturbances are examined by the direct transient computation. The readers are referred to Yang and Wang [19] for the numerical details and the check of grid-dependence and accuracy. The computations are carried out on the Super Computer SP2 of The University of Hong Kong.

3. Results and discussion

3.1. Solution structure and flow/temperature fields

At $\sigma = 0.02$, $Pr = 0.7$, $Dk = 300$, and $L1 = 28$, bifurcation structure is shown in Fig. 2 by varying $L2$ from -20 to 70. The u velocity component at (0.9, 0.14) is used as the state variable, enabling a clear visualization of all solution branches. Fig. 2(a) shows the whole solution structure form $L2 = -20$ to 70. Although there are only three solution branches labeled as $AS1$, $AS2$, and $S3$, solution structure is very complicated within $-15 \leqslant L2 \leqslant -8$ (Fig. 2(b)). In this range, the direction of buoyancy force is in negative R-direction while both the centrifugal force and Coriolis force act in the positive R-direction, the amplitudes of centrifugal force and Coriolis force are in same order of buoyancy force. Nonlinear counteraction of three forces generates a complex solution structure.

If $L2 \leqslant -14.5$ or $L2 \geqslant 63.1$, only one steady solution branch ($AS1$) exits and no limit point is found (Fig. 2(a)). Therefore, there is only one steady solution at each specified value of $L2$. Typical flow fields and temperature profiles within these two ranges are shown in Fig. 3. In Fig. 3(a), secondary flow on $AS1$ at $L2 = -17.0$ has 5-pair of counter-rotating vortices which are symmetric with respect to horizontal center plane. Among ten vortices, eight of them (two counter-rotating vortices are in the center region close to the outer wall, four vortices are in the four corners and two small vortices are in the center region of the duct) are called buoyancy-vortices [13]. They mainly result from action of buoyancy forces and are similar to the Dean-vortices [13] and Coriolis vortices [13,20] due to the action of centrifugal forces and Coriolis forces, respectively. The other two vortices located in the center region still maintain the characteristics of Ekman vortices. The buoyancy forces acting in negative R-direction are stronger than the centrifugal forces and Coriolis forces acting in the positive R-direction, resulting in the axial velocity peak and temperature peak close to the inner wall (Fig. 3(a)). If $L2 > 63.1$, multi-solution phenomenon disappears; only part of $AS1$ with no bifurcation point and no limit point is found. The typical solutions on various solution branch parts are shown in Fig. 3(b). The solution shown in Fig. 3(b) is the typical 2-cell solution with two Ekman vortices symmetrically distribute in the cross-section of the duct. By comparing the streamwise velocity profiles and temperature fields in Fig. 3(b) with those at $L2 = 0$ in Yang [20], it is observed that, while buoyancy force has less influence on temperature fields, two striking peaks of streamwise velocity along the upper and lower walls are formed due to its effect.

For a $L2$ value in $-14.5 < L2 < 63.1$, bifurcation phenomenon occurs. Because of the complexity of solution structure within the studied range of $L2$ values, it is difficult to present flow structure and temperature fields on each solution branch part. However, secondary flows of 4 solutions at $L2 = -11.7$ are shown in Fig. 4. It is expected that these solutions can enable us to obtain some insight of the flow structures of all the solutions within $-12.1 < L2 < -11.4$. It should be noted that 39 solutions co-exist at $L2 = -11.7$, the solutions shown in Fig. 4 are only the typical flow patterns. For detailed flow structures and temperature profiles at this para-

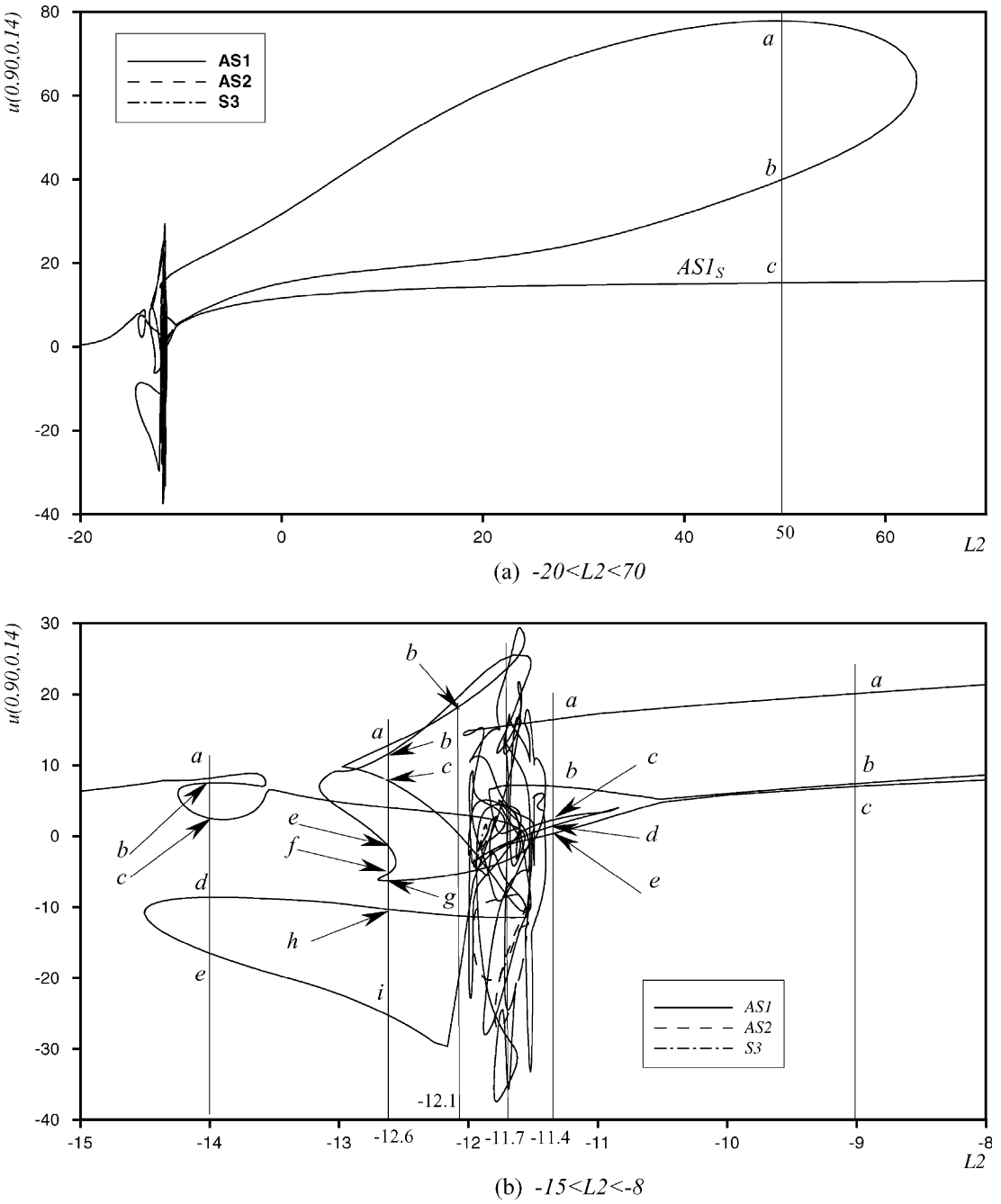

Fig. 2. Solution branches ($\sigma = 0.02$, $Pr = 0.7$, $Dk = 300$, and $L1 = 28$).

meter, readers are referred to Yang [20]. At $L2 = -11.7$, three forces (centrifugal, Coriolis and buoyancy forces) have the same order of magnitude. The non-linear combination of the three forces not only leads to a complicated solution structure, but also generates a complicated structure of the secondary flow (Fig. 4).

3.2. Stability of multiple steady solutions

A relatively comprehensive transient computation is made to examine the dynamic behavior and stability of typical steady solutions with respect to four sets of finite random disturbances with $d = 4\%$, 10%, 15%, and

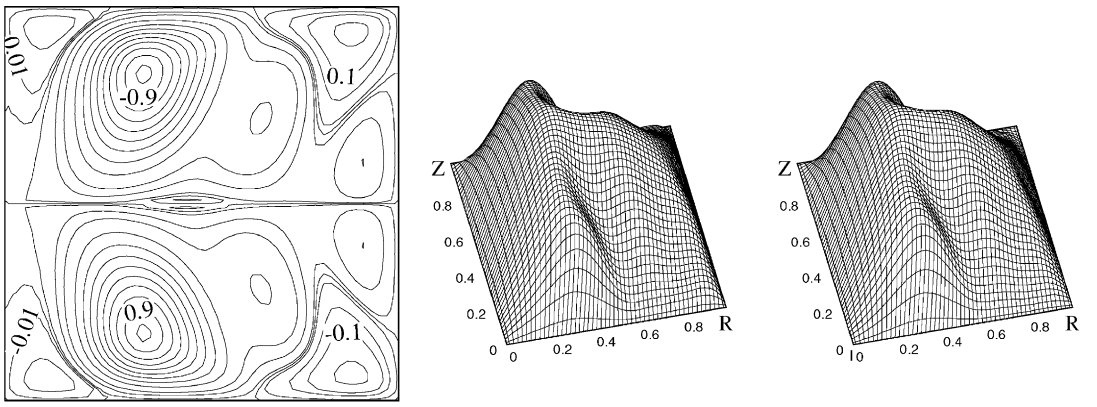

(a) *L2=-17.0* on *AS1* ($|\psi|_{max}$=7.14, w_{max} = 0.0606, t_{max} = 127.3)

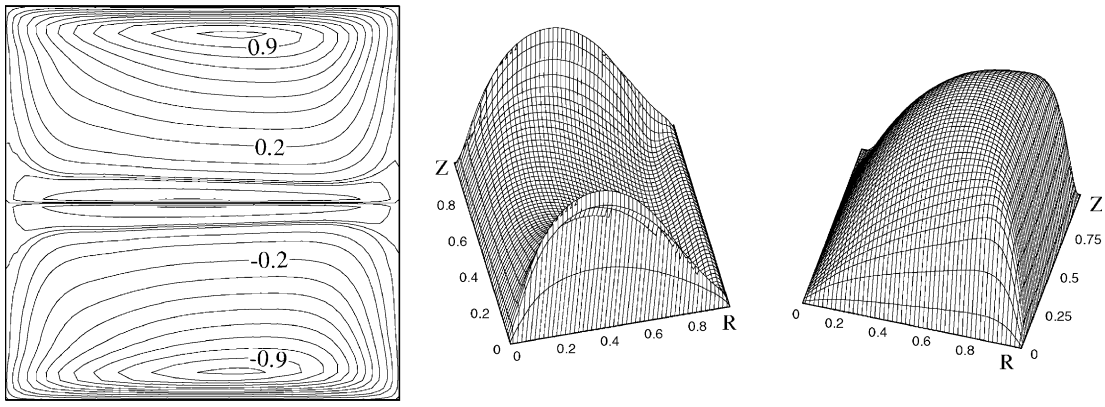

(b) *L2=65* on *AS1* ($|\psi|_{max}$=14.23, w_{max} = 0.0137, t_{max} = 8.9)

Fig. 3. Flow and temperature fields ($\sigma = 0.02$, $Pr = 0.7$, $Dk = 300$, and $L1 = 28$) (left—secondary flow, middle—streamwise velocity, right—temperature).

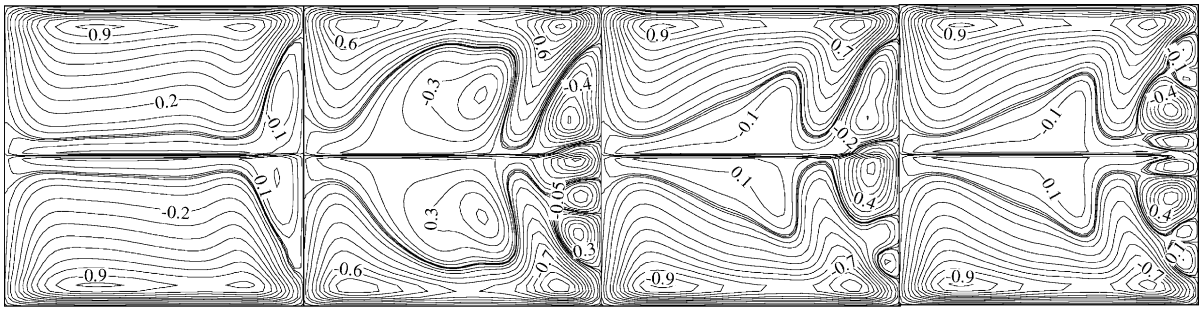

(a) *u(0.90,0.14)=-1.89* (b) *u(0.90,0.14)=4.33* (c) *u(0.90,0.14)=2.57* (d) *u(0.90,0.14)=-16.55*

Fig. 4. Typical secondary flow patterns at $L2 = -11.7$ ($\sigma = 0.02$, $Pr = 0.7$, $Dk = 300$, and $L1 = 28$).

40% respectively. Five types of dynamic responses are identified. They are stable 2-cell steady solution, stable multi-cell steady solution, periodic solution, symmetric-breaking oscillation led by sub-harmonic (Periodic doubling) bifurcation and temporal chaotic oscillation. Although nearly all types of the physically realizable solutions presented in the present work have already been reported in Yang and Wang [19], some new phe-

nomena of mixed convection motivate our further discussions. We find the co-existence of two types of temporal oscillations at certain values of $L2$. A new route to chaos, i.e., the sub-harmonic bifurcation, is also discovered in the present study.

According to the dynamic responses to finite random disturbances, seven sub-ranges are identified. To facilitate the discussion, some abbreviations are introduced. Within $-20 \leqslant L2 \leqslant 70$, possible physically realizable solutions can be in the form of stable steady 2-cell solution (S2), stable steady multi-cell solution (SM), temporal periodic oscillation (P), temporal chaotic oscillation (C) and temporal symmetric-breaking oscillation (SB). Fig. 5 details the ranges of these physically realizable solutions. It is observed that three stable multi-cell steady solutions (labeled as SM_1, SM_2, and SM_3 in Fig. 5, respectively.) co-exist at a specified value of $L2$ in sub-range $-14.5 < L2 < -13.6$ and temporal periodic solution co-exist with temporal chaotic solutions in sub-range $12.1 < L2 < -11.5$. We will describe the numerical simulation results within these seven sub-ranges in detail in follows. The results presented in this paper are those obtained from disturbance with $d = 10\%$ unless otherwise stated.

If $L2$ is less than -14.5 or larger than -10.2, random disturbances lead all solutions on various solution sub-branches to a unique stable steady solution. Fig. 6 typifies the responses of solutions to the finite random disturbances within these two sub-ranges. In the figures, the deviation of velocity components from their initial steady values (u', v') (Fig. 6(a)) or velocity itself (u, v) (Fig. 6(c)) is plotted against the time τ at (0.9, 0.14), (0.94, 0.1), and (0.96, 0.06) for $L2 = -15$ and $L2 = 50$, respectively. We plot both u- and v-velocity components for the first point (0.9, 0.14) while only u-velocity component is shown for the last two points. To facilitate the comparison, we use these four velocity components in all figures illustrating dynamic responses of the multiple solutions to the finite random disturbances. It is observed that all deviation velocities vanish after a short period of time.

Fig. 6(a) is a typical evolving process for $L2 \leqslant -14.5$. At $L2 = -15.0$, only one multi-cell steady solution has been found. It is observed that all oscillations vanish after a short period of time. The final state is multi-cell steady state similar to that shown in Fig. 6(b).

If $L2 > -10.2$, solutions on sub-branch $AS1_s$ (labeled in Fig. 2(a)) are the only stable ones. Fig. 6(c) shows the typical evolution process of the perturbed steady solutions on various sub-branches. At $L2 = 50$, the steady solution on the points a labeled in Fig. 2(a) are not stable and the solution on the point c (Fig. 2(a)) is stable. As an example, Fig. 6(c) gives the dynamic response of the steady solution on point a (at $L2 = 50$). The evolution process reaches the stable steady state quickly. After the evolution process reaches steady state, secondary flow pattern is 2-cell state as shown in Fig. 6(d).

Within $-14.5 < L2 < -13.6$, multiple stable steady solutions are revealed numerically. Fig. 7 illustrates the dynamic responses of three different steady solutions at $L2 = -14.0$ to random disturbances. Dynamic evolution in Fig. 7(a) uses sum of the solution on point a at $L2 = -14.0$ in Fig. 2(b) and the random disturbances as the initial condition. It is observed that the disturbances disappear after a short period of time. The final state is the multi-cell state of Fig. 7(b). Fig. 7(c) is the dynamic response of steady solution on point d at $L2 = -14.0$ in Fig. 2(b). It is observed that the dynamic evolution reaches the steady state at $\tau \approx 1.2$. The flow and temperature fields of the final steady state are the multi-cell state shown in Fig. 7(d). Another stable steady solution at $L2 = -14.0$ is the solution on point e at $L2 = -14.0$ in Fig. 2(b). Fig. 7(e) shows the evolution process of this solution. It clearly illustrates that the finite random disturbances lead the solution on point e at $L2 = -14.0$ in Fig. 2(b) return to the original state after a short period of time. The secondary flow pattern of the final evolution is shown in Fig. 7(f).

It should be pointed out that, in spite of three stables steady solutions at $L2 = -14.0$, only two stable steady solutions co-exist in the range of $-14.5 < L2 < -14.2$. At $L2 = -14.2$, limit point $AS1^2$ marked in Fig. 2(b) leads one of the stable solution sub-branch to disappear for $L2 < -14.2$.

Within $-13.6 \leqslant L2 \leqslant -12.1$, finite random disturbances lead the solutions on all solution branches to a temporal periodic state. The extensive results of direct transient calculation prove that, at certain value of $L2$, temporal periodic oscillations are the only physically realizable solution within $-13.6 \leqslant L2 \leqslant -12.1$. The typical dynamic evolution of solutions is shown in Fig. 8(a). The figure shows the evolution process of a steady solution at $L2 = -12.1$ to random disturbances. This steady solution is on the same sub-branch with the point a labeled at $L2 = -12.6$ in Fig. 2(b) [labeled as point b at $L2 = -12.1$ in Fig. 2(b)].

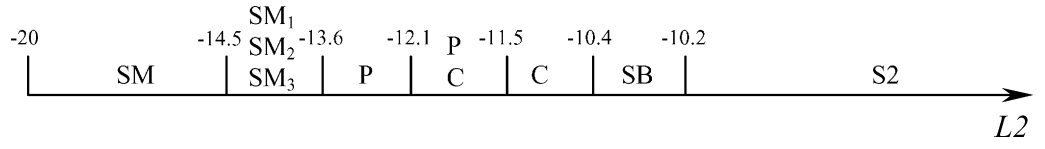

Fig. 5. Possible physically realizable solutions ($\sigma = 0.02$, $Pr = 0.7$, $Dk = 300$, and $L1 = 28$).

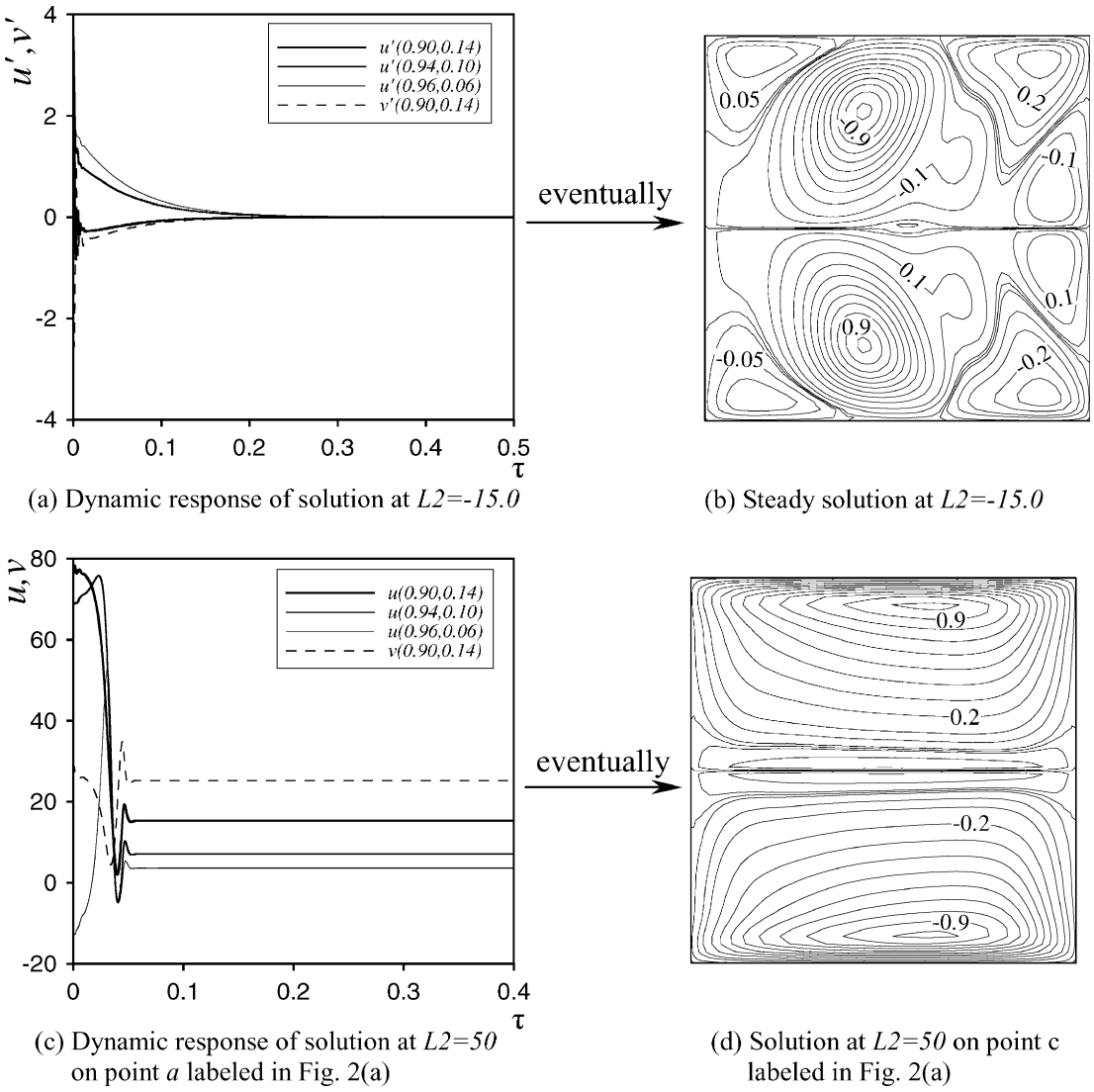

(a) Dynamic response of solution at *L2=-15.0*

(b) Steady solution at *L2=-15.0*

(c) Dynamic response of solution at *L2=50* on point *a* labeled in Fig. 2(a)

(d) Solution at *L2=50* on point c labeled in Fig. 2(a)

Fig. 6. Evolution of solution to stable steady solution ($\sigma = 0.02$, $Pr = 0.7$, $Dk = 300$, and $L1 = 28$).

Some typical secondary flow patters for Fig. 8(a) are detailed in Fig. 8(b)–(g) within one period of τ. Fig. 8(b)–(g) begin with the symmetric 12-cell secondary flow pattern at $\tau = 0.964$ and end with the similar secondary flow pattern at $\tau = 1.029$. It is observed that, the secondary flows change from symmetric 12-cell state to symmetric 14-cell state gradually as τ increases. While the large changes are in central region of the cross-section, some small changes are also on the forms of buoyancy vortices close to the outer wall and in four corners of the cross-section. Smaller magnitude of oscillation mentioned above (Fig. 8(a)) is due to the fact that four velocity components shown in the figure are located close to the outer wall.

Within $-12.1 \leqslant L2 \leqslant -11.5$, random disturbances lead the steady solutions on various solution sub-branches to two types of temporal oscillations. One is periodic solution and another is chaotic oscillation. The typical dynamic responses to finite random disturbance of steady solutions within $-12.1 \leqslant L2 \leqslant -11.5$ are shown in Fig. 9. Fig. 9 illustrates four temporal evolution processes at $L2 = -11.7$. Different temporal solutions are from the steady solutions on different sub-branches perturbed by random disturbances. The random disturbances lead the steady solution shown in Fig. 4(a) to temporal chaotic oscillation (Fig. 9(a)) while the dynamic evolution process of the steady solution shown in Fig. 4(b) is temporal periodic oscillation

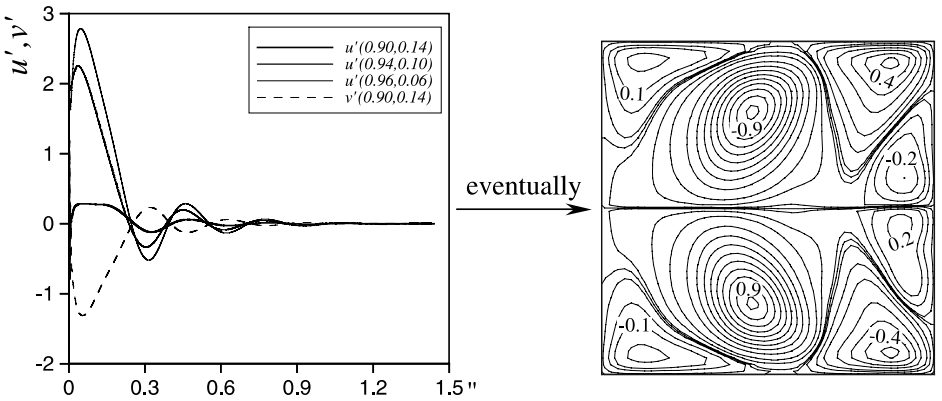

(a) *L2=-14.0* on point *a* labeled in Fig. 2(b) (b) *u(0.90,0.14)=8.137*

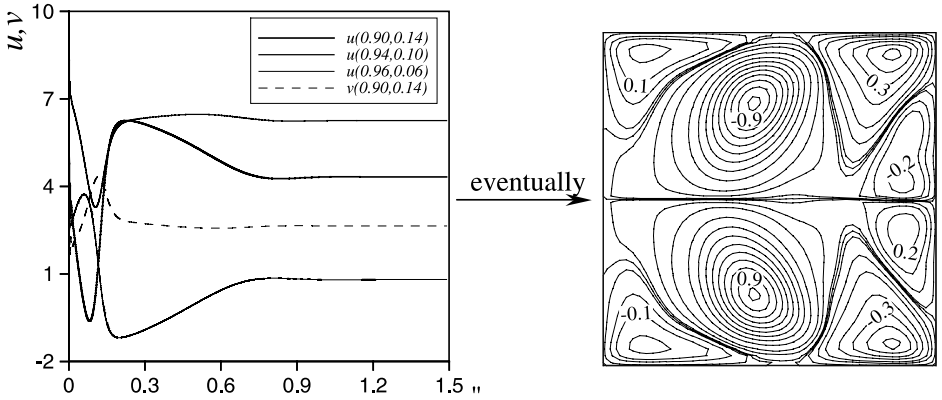

(c) *L2=-14.0* on point *d* labeled in Fig. 2(b) (d) *u(0.90,0.14)=2.493*

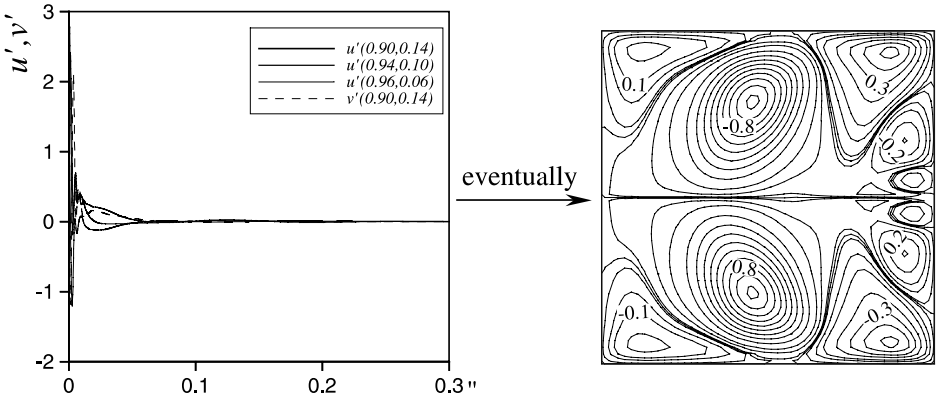

(e) *L2=-14.0* on point *e* labeled in Fig. 2(b) (f) *u(0.90,0.14)=-16.52*

Fig. 7. Dynamic responses of the steady solutions at $L2 = -14$ to finite random disturbances: Co-existence of three stable steady multi-cell states ($\sigma = 0.02$, $Pr = 0.7$, $Dk = 300$, and $L1 = 28$).

(Fig. 9(b)). For steady solutions shown in Fig. 4(c) and (d), the final states of two evolving processes shown in Fig. 9(c) and (d) are also chaotic oscillation and periodic oscillation, respectively. But temporal oscillations in Fig. 9(c) and (d) are different from those in Fig. 9(a) and (b) in the way that both evolution processes in Fig. 9(c) and (d) are very long before reaching final chaotic oscillation or periodic oscillation states.

If the physically realizable solution is in chaotic oscillation as shown in Fig. 9(a), flow field also oscillates

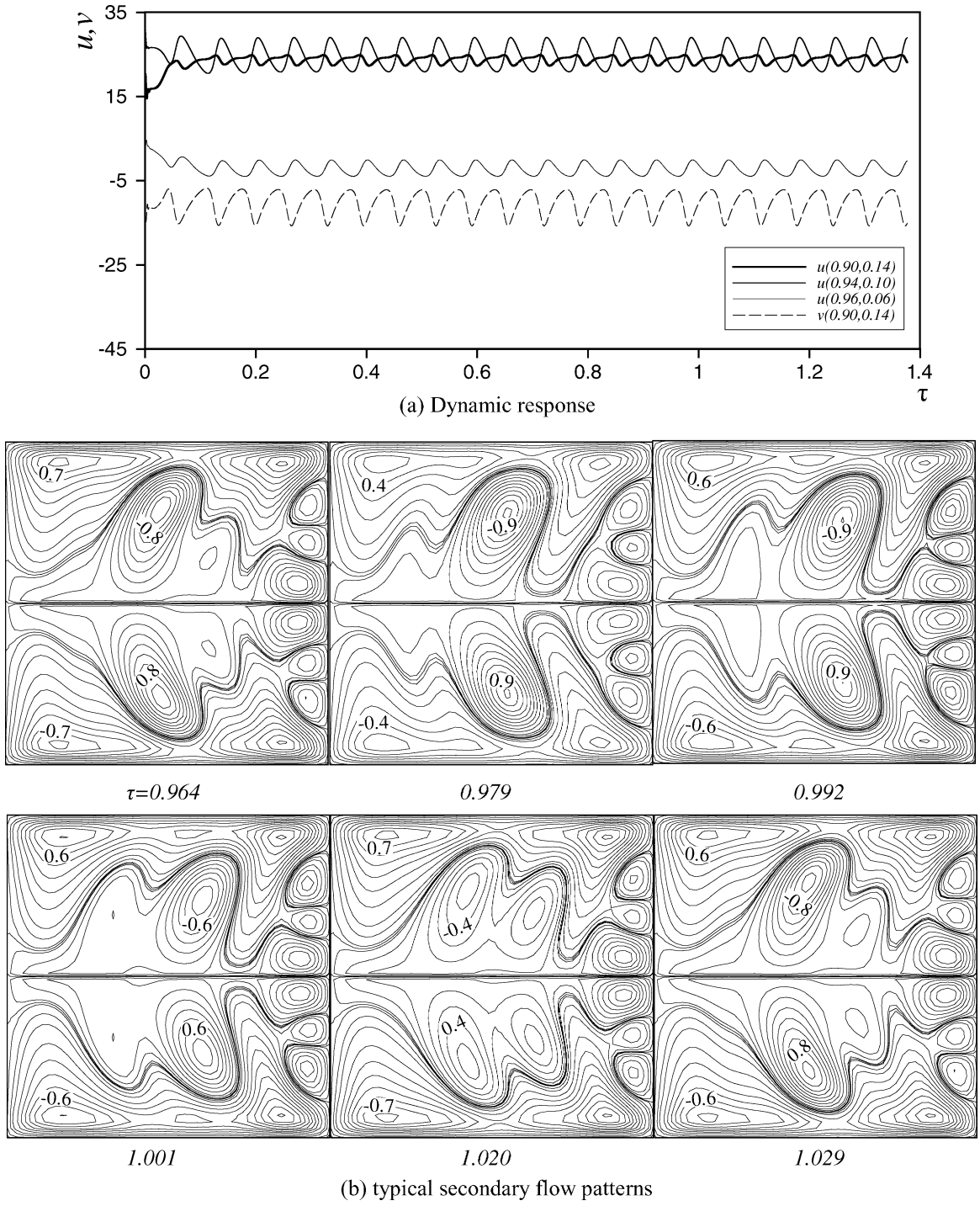

Fig. 8. Dynamic response of solution b at $L2 = -12.1$ labeled in Fig. 2(b) to finite random disturbances: periodic oscillation and typical secondary flow patterns in one period (period = 0.065; $\sigma = 0.02$, $Pr = 0.7$, $Dk = 300$, and $L1 = 28$).

chaotically with time τ. Fig. 10 shows some secondary flow patterns for the case of Fig. 9(a). First secondary flow pattern in Fig. 10(a) is at $\tau = 0.786$ and last one in Fig. 10(f) is at $\tau = 0.833$.

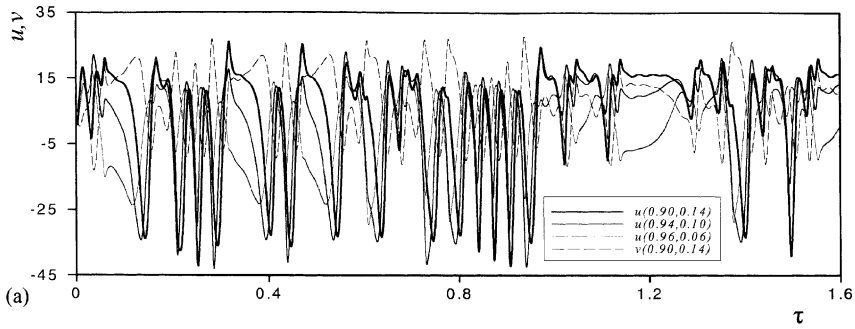

(a) Solution shown in Fig 4(a)

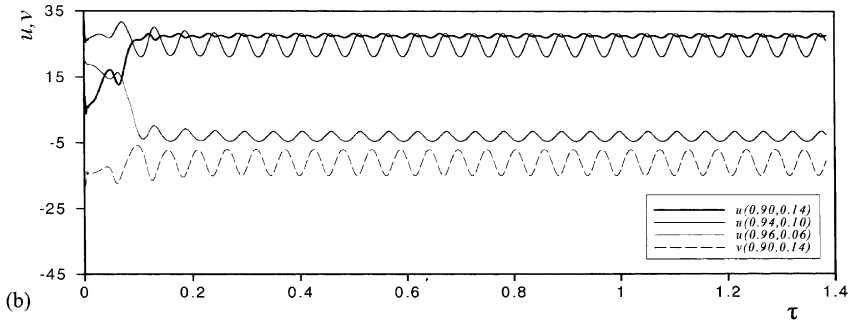

(b) Solution shown in Fig. 4(b)

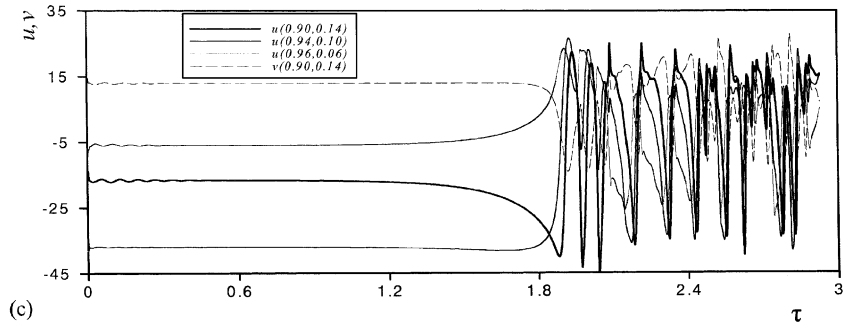

(c) Solution shown in Fig. 4(c)

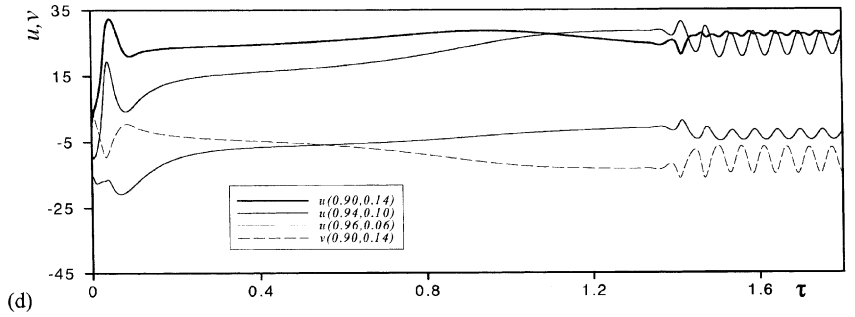

Fig. 9. Dynamic responses of the solutions at $L2 = -11.7$ to finite random disturbances: co-existence of periodic and chaotic oscillations ($\sigma = 0.02$, $Pr = 0.7$, $Dk = 300$, and $L1 = 28$).

For periodic oscillation at $L2 = -11.7$ (Fig. 9(b)), secondary flow patterns have the similar multi-cell forms as those in Fig. 8(b)–(g). Within one period of time, the multi-cell secondary flows change in the same way as that for periodic solution at $L2 = -12.1$ discussed above.

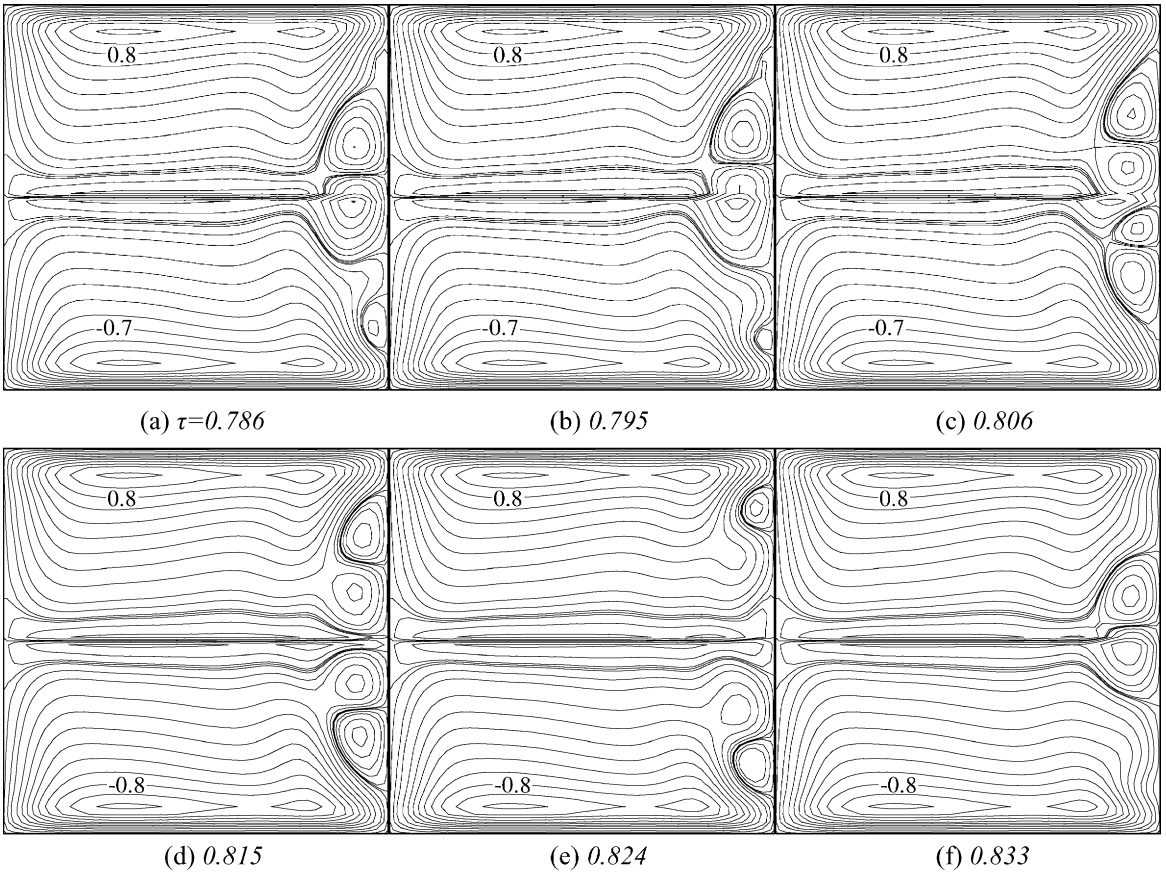

Fig. 10. Typical secondary flow patterns of chaotic oscillation for the case in Fig. 9(a) ($\sigma = 0.02$, $Pr = 0.7$, $Dk = 300$, $L1 = 28$, and $L2 = -11.7$).

The essential differences between two types of oscillations shown in Fig. 9(a) and (b) are discovered by comparing the secondary flow patterns in Fig. 10 with those in Fig. 8(b)–(g). First, secondary flow patterns of periodic oscillation maintain the symmetric multi-cell forms; secondary flow patterns of chaotic oscillation change between symmetric and asymmetric patterns (Fig. 10). Second, secondary flow patterns of periodic oscillation are complex symmetric multi-cell. At least twelve vortices are observed from Fig. 8(b)–(g). But secondary flow patterns of chaotic oscillation are relative simpler. Maximal eight vortices are generated (Fig. 10(a) to (f)). In addition, in the case of chaotic oscillation, only buoyancy vortices close to the outer wall are observed. But in the case of periodic oscillation, buoyancy vortices are found everywhere in the duct cross-section. Third, in the case of periodic oscillation, significant changes are in the central region of the cross-section. But in the case of chaotic oscillation, buoyancy vortices near the outer wall changes significantly along with the time, two Ekman vortices in the central region maintain approximately unchanged during the chaotic oscillation.

If $L1$ increases further from $L2 = -11.5$, the periodic solution disappears. Chaotic oscillation exists uniquely in sub-range of $-11.5 \leqslant L2 \leqslant -10.4$. The typical dynamic responses to finite random disturbance of steady solutions within this sub-range are shown in Fig. 11. By comparing Fig. 11 with chaotic oscillations shown in Fig. 8(a), it is not difficulty to observe that the chaotic oscillation within $-11.5 \leqslant L2 \leqslant -10.4$ has the same characteristic of that in sub-range $-12.1 \leqslant L2 \leqslant -11.5$.

As discussed above, the physical realizable solution is chaotic oscillation within $-11.5 \leqslant L2 \leqslant -10.4$. If $L2 > -10.2$, steady stable solution is found. The transition from chaotic oscillation to the stable steady solution takes place in sub-range $-10.4 < L2 \leqslant -10.2$. Temporal oscillation with intermittency and the sudden shift from the stable steady solutions to the chaotic solutions that

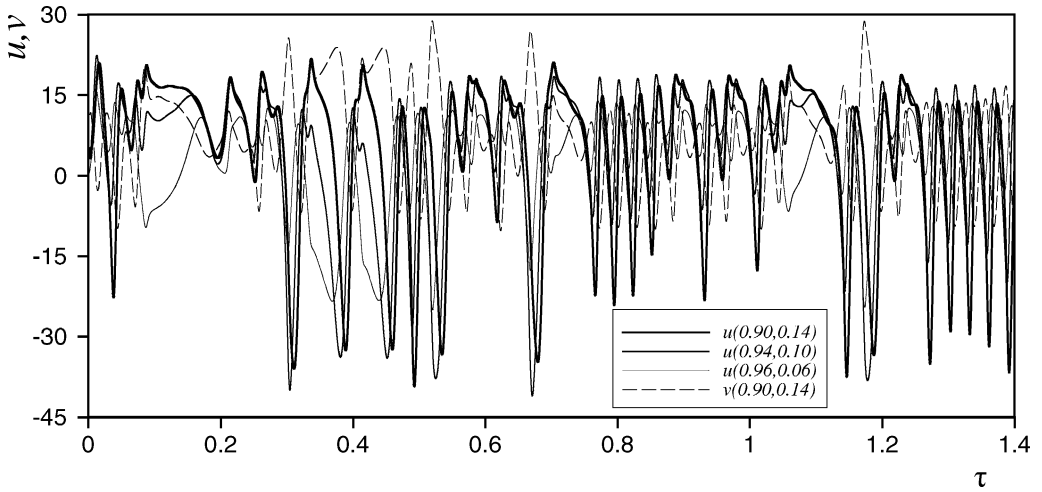

Fig. 11. Dynamic response of the solution on point c at $L2 = -11.4$ labeled in Fig. 2(c) to finite random disturbances: chaotic oscillation ($\sigma = 0.02$, $Pr = 0.7$, $Dk = 300$, $L1 = 28$, and $L2 = -11.4$).

was reported in [16,20] are not found. An asymmetric mode of oscillation led by sub-harmonic bifurcation is observed within $-10.4 < L2 \leqslant -10.2$. It is confirmed that sub-harmonic bifurcation serves the way for onset of chaos. Since the transitional oscillation is important towards chaotic oscillation, detailed observation of temporal solutions is made within $-10.4 < L2 \leqslant -10.2$. Fig. 12 shows symmetric/asymmetric mode of oscillation at four different value of $L2$. It demonstrates that, as $L2$ decreases from −10.2, temporal oscillation changes from periodic to non-periodic and develops chaos gradually. The corresponding power spectra in Fig. 12 are shown in Fig. 13. The observed sequence of instabilities is as follows: Hopf bifurcation leads to the transition from stable steady solution to the temporal periodic oscillation at $L2 = -10.2$ (Figs. 12(a) and 13(a)). It should be noted that the frequency labeled as f_1 in Fig. 13(a) appears for all the velocity components, pressure and temperature at all points in the cross-section. The amplitudes of the temporal oscillation are different for the velocity components; pressure and temperature at various positions, but the frequency are invariant. At $L2 = -10.25$, a second frequency labeled as f_2 in Fig. 13(b) appears in the spectrum (throughout the whole cross-section) as show in Figs. 12(b) and 13(b). By comparing the values of f_1 and f_2 in Fig. 13(b), it is not difficult to obtain that $f_2 = (1/2)f_1$, indicating sub-harmonic bifurcation or period-doubling bifurcation. As $L2$ decreases further, at $L2 = -10.30$, a second sub-harmonic bifurcation doubles the period of temporal oscillation again and third frequency labeled as $f_3 (f_3 = (1/4)f_1)$ (Fig. 13(c)) appears. From Fig. 13(c), it is observed that the peaks at f_2 and f_3 are relatively weak, but they grow continuously as $L2$ decreases. At $L2 = -10.35$, the oscillations become non-periodic, the spectrum shows many closely spaced peaks (Fig. 13(d)). The broadband of the spectra indicates the onset of chaos.

The onset of chaos through the way of sub-harmonic bifurcation was observed experimentally in Gollub and Benson [3] for the problem of thermal convection between flat horizontal plates. Lipps [1], McLaughlin and Orszag [2], and Clever and Busse [21] made numerical simulations for the same problem. Some of the temporal oscillation modes reported appear identical with the mode in the present work. Obviously, the problem studied by Gollub and Benson [3], Lipps [1], McLaughlin and Orszag [2], and Clever and Busse [21] are different from that in the present work. But the two problems share a common ground: both of them concern the flows under the influence of buoyancy force. The strong resemblance of the ways to chaos between the two problems suggests that the buoyancy forces enhances sub-harmonic bifurcation and suppress the intermittency.

4. Concluding remarks

The numerical method is employed to study 2-D hydrodynamically and thermally fully developed flow and heat transfer in rotating curved square ducts. Although flow and heat transfer occurring in real rotating curved ducts may be 3-D. A 2-D model is still useful for a fundamental understanding of rotating curved duct flows.

The governing differential equations are discretized by finite volume method. The discretization equations are solved by Euler–Newton continuation by using $L2$, arclength or local variable as the control parameter.

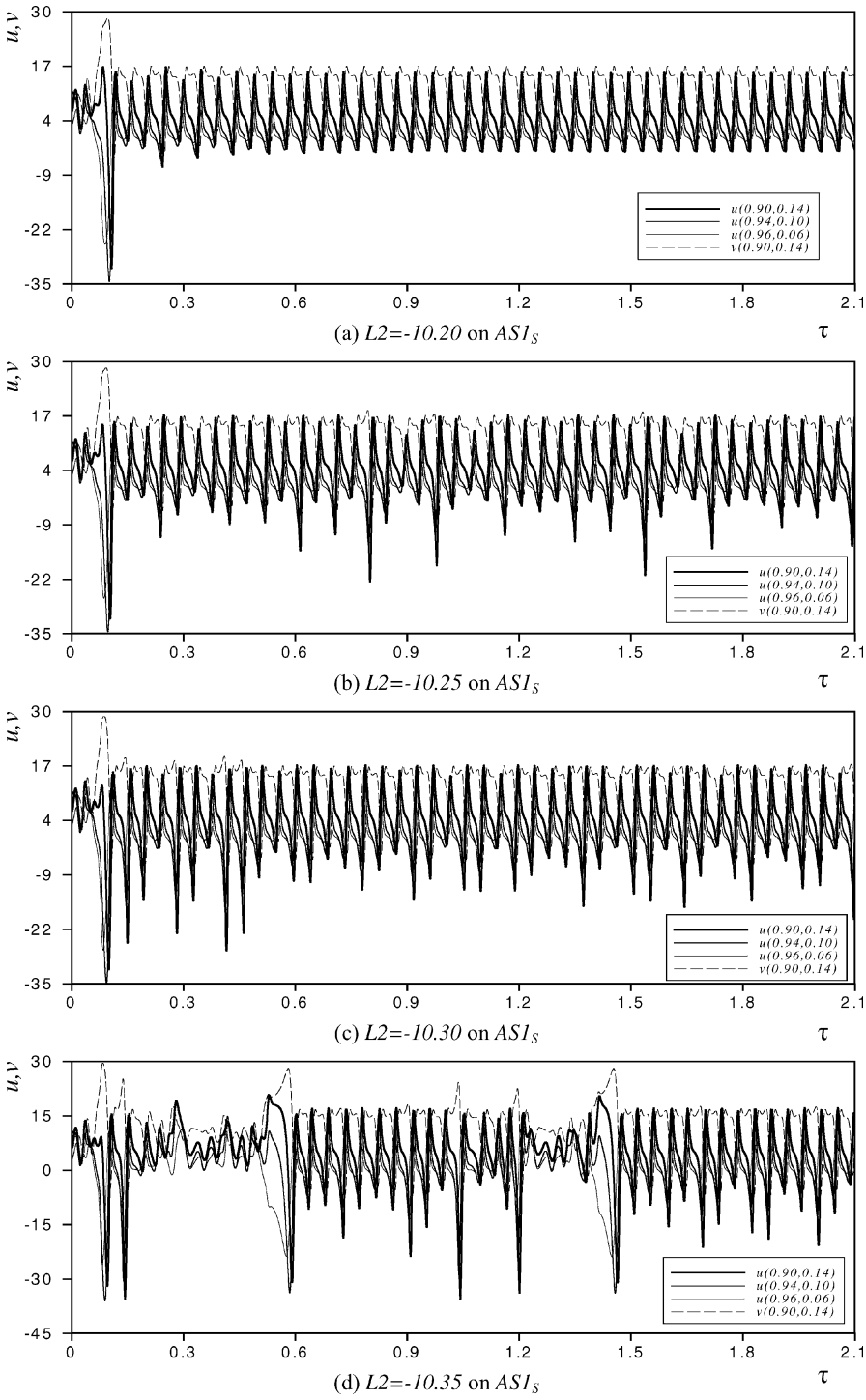

Fig. 12. Dynamic response of the solution to finite random disturbances: symmetric-breaking oscillation ($\sigma = 0.02$, $Pr = 0.7$, $Dk = 300$, and $L1 = 28$).

Bifurcation point detection and the branch switching technique described in Seydel [17,18] are used to unfold various solution branches. Although only three steady solution branches are found within $-20 < L2 < 70$, the

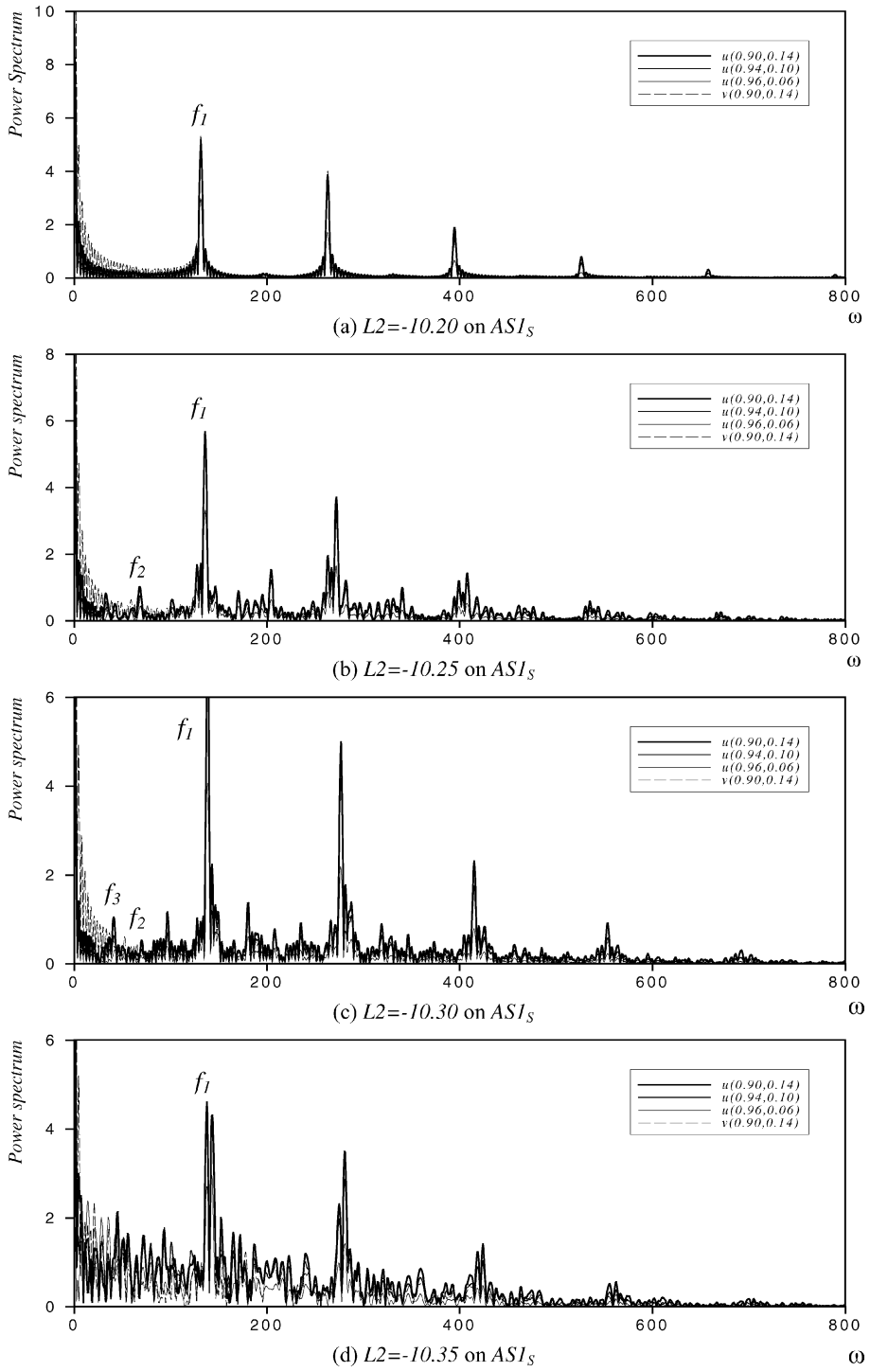

Fig. 13. Power spectra of the temporal series shown in Fig. 12 ($\sigma = 0.02$, $Pr = 0.7$, $Dk = 300$ and $L1 = 28$).

very complicated solution structure exists within $-14 < L2 < 10$ due to large number of limit points and bifurcation points in this region.

On different steady solution branches, steady flow and temperature fields have different structures. 2- to 14-cell symmetric/asymmetric flows are found.

Complicated structure of solutions and multi-cell flows within $-14 < L2 < 10$ forecasts the onset of instabilities.

Dynamic responses of steady multiple solutions to finite random disturbances are examined by direct transient computation. Stability of solutions on various solution branches changes as value of $L2$ changes. Five types of physically realizable solutions are identified in seven sub-ranges of $L2$. The first sub-range is $-20 \leqslant L2 \leqslant -14.5$, where finite random disturbances lead only steady solution at any fixed $L2$ to a stable multi-cell steady state. Within $-14.5 < L1 < -13.6$, multiple stable steady solutions are found. There are two or three stable multi-cell steady solutions at fixed value of $L2$ (depending on the value of $L2$). Third sub-range covers the range $-13.6 < L2 \leqslant -12.1$ where all steady solutions evolve to temporal periodic solution. In fourth sub-range ($-12.1 \leqslant L2 < -11.50$), two types of temporal oscillation co-exist. Finite random disturbances lead some steady solutions to a periodic oscillation and other solutions at the same value of $L2$ to a chaotic oscillation. Fifth sub-range is from $L2 = -11.50$ to -10.4 where all the solutions respond to finite random disturbances in the form of chaotic temporal oscillation. Sixth sub-range ($-10.4 < L2 \leqslant -10.2$) serves as the transition range from stable steady state to chaotic oscillation, where sub-harmonic bifurcation leads the temporal oscillation from periodic at $L2 = -10.2$ to symmetry-breaking oscillation at $L2 < -10.2$. In last sub-range $L2 > -10.2$, one solution branch becomes stable again and stable steady solutions become the 2-cell state as $L2$ increases from $L2 = -10.1$ to 70.

The complicated instability characteristics summarized above suggest that flows studied here are in the transition region from laminar to turbulent flows. Coexistence of different types of stable solutions (physical realizable solutions) implies that, when flow is in such transition region, the flow structure is very complicated and they may change in different ways in time. At the specific values of flow parameters, the flows may have different features, i.e. periodic oscillating or chaotic oscillating flows.

Acknowledgements

The financial support from the Research Grants Council of Hong Kong (RGC, Project no: HKU7086/00E), the CRCG and the Outstanding Young Researcher Award of the University of Hong Kong to LW is gratefully acknowledged.

References

[1] F.B. Lipps, Numerical simulation of three-dimensional Bènard convection in air, J. Fluid Mech. 75 (1976) 113–148.
[2] J.B. McLaughlin, S.A. Orszag, Transition from periodic to chaotic thermal convection, J. Fluid Mech. 122 (1982) 123–142.
[3] J.P. Gollub, S.V. Benson, Many routes to turbulent convection, J. Fluid Mech. 100 (1980) 449–470.
[4] H. Ludwieg, Die ausgebildete kanalströmung in einem rotierenden system, Ing. -Arch. Bd. 19 (1951) 296–308.
[5] H. Miyazaki, Combined free and forced convective heat transfer and fluid flow in a rotating curved circular tube, Int. J. Heat Mass Transfer 14 (1971) 1295–1309.
[6] H. Miyazaki, Combined free and forced convective heat transfer and fluid flow in a rotating curved rectangular tubes, J. Heat Transfer 95 (1973) 64–71.
[7] L. Wang, K.C. Cheng, Flow transitions and combined free and forced convective heat transfer in a rotating curved circular tube, Int. J. Heat Mass Transfer 39 (1996) 3381.
[8] P. Daskopoulos, A.M. Lenhoff, Flow in curved ducts. Part 2. Rotating ducts, J. Fluid Mech. 217 (1990) 575–593.
[9] O.J.E. Matsson, P.H. Alfredsson, Curvature- and rotation-induced instabilities in channel flow, J. Fluid Mech. 210 (1990) 537–563.
[10] O.J.E. Matsson, P.H. Alfredsson, The effect of spanwise system rotation on Dean vortices, J. Fluid Mech. 274 (1994) 243.
[11] Y. Guo, W.H. Finlay, Splitting, merging and wavelength selection of vortices in curved and/or rotating channel flow due to Eckhaus instability, J. Fluid Mech. 228 (1991) 661–691.
[12] L. Wang, K.C. Cheng, Flow in curved channels with a low negative rotating speed, Phys. Rev. E 51 (1995) 1155.
[13] L. Wang, K.C. Cheng, Flow transitions and combined free and forced convective heat transfer in rotating curved channels: The case of positive rotation, Phys. Fluids 6 (1996) 1553–1573.
[14] M. Selmi, K. Nandakumar, W.H. Finlay, A bifurcation study of viscous flow through a rotating curved duct, J. Fluid Mech. 262 (1994) 353–375.
[15] M. Selmi, K. Nandakumar, Bifurcation study of flow through rotating curved ducts, Phys. Fluid 11 (1999) 2030–2043.
[16] T. Yang, L. Wang, Solution structure and stability of viscous flow and heat transfer in curved channels, ASME C: J. Fluid Eng. 123 (2001) 863–868.
[17] R. Seydel, Branch switching in bifurcation problems for ordinary differential equations, Numer. Math. 41 (1983) 91–116.
[18] R. Seydel, Practical Bifurcation and Stability Analysis: From Equilibrium to Chaos, Springer-Verlag, New York, 1994.

[19] T. Yang, L. Wang, Microscale flow bifurcation and its macroscale implications in periodic porous media, Computat. Mech. 26 (2000) 520–527.
[20] T. Yang, Multiplicity and stability of flow and heat transfer in rotating curved ducts, Ph.D. thesis, Department of Mechanical Engineering, The University of Hong Kong, 2001.
[21] R.M. Clever, F.H. Busse, Nonlinear oscillatory convection, J. Fluid Mech. 176 (1987) 403–417.